Flame Acceleration and Deflagration-to-Detonation Transition of Hydrogen-Oxygen in Microchannels

R. W. Houim*, V. N. Gamezo, and E. S. Oran

Laboratories for Computational Physics and Fluid Dynamics,
Naval Research Laboratory, Washington, DC 20375
**NRC/NAS Postdoctoral Research Associate*

1 Introduction

Hydrogen-air mixtures can be prone to detonation [1], which presents significant safety hazards for their use as a practical fuel. Despite the long history of research, fundamental mechanisms of deflagration-to-detonation transition (DDT) are still not completely understood. Many DDT mechanisms proposed involve the formation of hot spots [1–5] that contain reactivity gradients. Ignition of a hot spot produces a spontaneous reaction wave that propagates through the reactivity gradient and generating either a decoupled shock and flame or a detonation, depending on the size of the hot spot and the shape of the reactivity gradient.

A different DDT mechanism was recently observed in numerical simulations of high-speed turbulent [6] and laminar [7] flames when the velocity of the burned products becomes sonic with respect to the flame. When this condition is met, the deflagration is said to be choked and pressure begins to rise locally near the flame surface. This, in turn, increases the chemical reaction rate. Feedback between the increasing pressure and the increasing chemical reaction rate may lead to a runaway condition and transition the flame to a detonation.

Though DDT in experiments usually occurs in the presence of turbulent flames, acceleration of laminar flames can lead to detonation as well. One example is flame propagation in a thin channel [8] when boundary layers become a large fraction of the cross-sectional area. Flame acceleration in these channels is dominated by flame stretching due to boundary-layer effects; turbulence does not play a significant role. Stretching of the flame increases its surface area and the total rate of chemical energy release. Feedback between flame stretch and the increasing chemical energy release may lead to detonation.

Two different mechanisms of DDT have been observed from numerical simulations of flame acceleration in thin channels [9, 10]. Oran *et al.* [9] found that a detonation developed in a region with a temperature gradient near the channel wall. Ivanov *et al.* [10] observed pressure building up as a shock that formed at the leading edge of the flame and transitioned to a detonation. The mechanism of this pressure buildup and transition to detonation could be similar to runaway mechanisms mentioned above [6, 8], though more analysis is needed.

Recent experiments [11] have successfully achieved DDT in sub-millimeter gaps. These experiments show that radially expanding stoichiometric ethylene/oxygen flames can undergo DDT even though they are confined in a 260 μm-high gap. Transition to detonation occurred at atmospheric conditions without preheating the gas mixture or the smooth PMMA slabs forming the gap.

Here we analyze mechanisms of DDT in thin channels using two-dimensional (2D) numerical simulations of flame acceleration and DDT in H_2/O_2 mixtures. We simulate small rectangular and circular channels, 0.5 mm in height, by solving the compressible Navier-Stokes equations with a detailed chemical reaction mechanism.

2 Numerical Model and Computational Setup

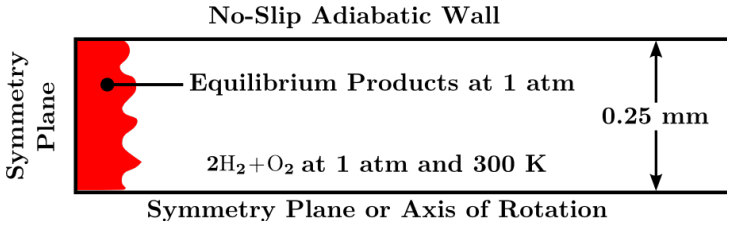

Figure 1: Initial and boundary conditions for the simulations performed in study.

The two-dimensional reactive Navier-Stokes equations with variable specific heat are used to model the flame acceleration and DDT of a stoichiometric mixture of hydrogen and oxygen:

$$\frac{\partial \mathbf{U}}{\partial t}+\frac{\partial \mathbf{F}}{\partial x}+\frac{\partial \mathbf{G}}{\partial y}+\eta\frac{\mathbf{G}_r}{y}=\frac{\partial \mathbf{F}_v}{\partial x}+\frac{1}{y^\eta}\frac{\partial y^\eta \mathbf{G}_v}{\partial y}+\mathbf{S}, \tag{1}$$

where η is a coordinate system selector that is zero in Cartesian coordinates and unity for axisymmetric coordinates. The vectors in Eq. (1) are given by:

$$\mathbf{U}=\begin{bmatrix}\rho Y_1\\ \vdots\\ \rho Y_N\\ \rho u\\ \rho v\\ \rho E\end{bmatrix},\quad \mathbf{F}=\begin{bmatrix}\rho u Y_1\\ \vdots\\ \rho u Y_N\\ \rho u^2+p\\ \rho uv\\ u(\rho E+p)\end{bmatrix},\quad \mathbf{G}=\begin{bmatrix}\rho v Y_1\\ \vdots\\ \rho v Y_N\\ \rho vu\\ \rho v^2+p\\ v(\rho E+p)\end{bmatrix},\quad \mathbf{G}_r=\begin{bmatrix}\rho v Y_1\\ \vdots\\ \rho v Y_N\\ \rho vu\\ \rho v^2\\ v(\rho E+p)\end{bmatrix},$$

$$\mathbf{F}_v=\begin{bmatrix}-J_{x,1}\\ \vdots\\ -J_{x,N}\\ \sigma_{xx}\\ \sigma_{xy}\\ u\sigma_{xx}+v\sigma_{xy}-q_x\end{bmatrix},\quad \mathbf{G}_v=\begin{bmatrix}-J_{y,1}\\ \vdots\\ -J_{y,N}\\ \sigma_{yx}\\ \sigma_{yy}\\ u\sigma_{yx}+v\sigma_{yy}-q_y\end{bmatrix},\quad \mathbf{S}=\begin{bmatrix}\dot{\omega}_1\\ \vdots\\ \dot{\omega}_N\\ 0\\ 0\\ 0\end{bmatrix},$$

where ρ, u and v, Y_i, E, p represent the density, velocity components, mass fraction of species i, specific total energy including chemical energy, and pressure, respectively. The ideal gas equation of state is used to relate pressure, chemical composition, temperature, and density:

$$p=\rho R_u T\sum_{i=1}^{N}\frac{Y_i}{Mw_i}, \tag{2}$$

where Mw_i is the molecular weight of species i and R_u is the universal gas constant. The mass production rate of chemical species i, mass diffusion flux of species i, deviatoric stress tensor, and diffusion heat flux vector are represented by $\dot{\omega}_i$, $\mathbf{J}_i$, $\boldsymbol{\sigma}$, and $\mathbf{q}$, respectively. Details on how these parameters are computed in this model can be found in Houim and Kuo [12].

Input includes a detailed chemical reaction mechanism [13] and the corresponding specific heat polynomials and Lennard-Jones parameters needed to represent the molecular transport coefficients. This chemical reaction mechanism involves 23 reversible elementary chemical reactions among the 8 species H_2, O_2, H_2O, H, O, OH, HO_2, and H_2O_2. Although this mechanism does not properly reproduce the cellular structure of hydrogen/air detonations [14], it has been validated for a variety of other conditions including high-pressure (around to 20 atm) deflagrations [13]. For modeling DDT, it is important for the mechanism to reproduce the flame speed and ignition delay over as wide range of pressures and temperatures as possible.

The governing equations are solved using an operator-split approach with a fifth-order low-dissipation and quasi-conservative approach for the hyperbolic terms [12] and second-order conservative differencing for the viscous and diffusion terms. The Paramesh library [15] is used for adaptive mesh refinement. The computational cell size at the finest level of refinement is $\Delta x = 3.47$ μm. Hyperbolic terms are integrated in time using second-order Runge-Kutta [16] and a directionally unsplit approach. The viscous and diffusion terms are integrated in time using Runge-Kutta-Chebyshev [17] with six stages on average. The overall time-step size is determined using a CFL number of 0.5 based solely on the hyperbolic terms. Further details on the numerical methods and an extensive suite of verification and validation tests including premixed deflagrations, Chapman-Jouget detonations, and cellular detonations can be found in Houim and Kuo [12].

The initial conditions are shown in Fig. 1. A 500 μm-high channel is filled with a stoichiometric mixture of hydrogen and oxygen at a pressure of 1 atm and a temperature of 300 K. The walls of the channel are no-slip and adiabatic to avoid quenching of the flame. The symmetry conditions applied on the left and bottom sides of the domain reduce computational expense. The bottom boundary condition is changed from a symmetry plane to an axis of rotation and η is changed from 0 to 1 in Eq. (1) for channels with a circular cross-section. Boundary conditions at the exit are simply extrapolated because acoustic waves generated from the flame do not reach the exit. The initial flame surface is approximated as a discontinuity between the reactants and constant-pressure equilibrium products placed roughly 500 μm from the left side of the computational domain.

3 Results

The evolution of the flame as it accelerates and transitions to detonation is shown in Fig. 2. Pressure profiles along the centerline of the channel are shown in Fig. 3. The initial phase of flame acceleration is similar for both the Cartesian and axisymmetric channels. Initially the flame starts burning and induces downstream fluid motion in the channel. Burned products cannot leave the domain because of left symmetry plane. Instead, they create fluid motion and a boundary layer ahead of the flame. The boundary layer creates a nonuniform velocity profile with the highest axial velocity in the center of the channel. This stretches the flame and gives it a finger-like shape. As the flame stretches, the rate of chemical energy release increases and the flow accelerates and stretches the flame even more. The result is very large accelerations of the flame. At a time of 166 μs, the absolute flame speed is $\sim$650 m/s in the Cartesian channel. The flame accelerates more quickly in the circular channel, by around a factor of 3.17, due to a combination of a higher flame surface area to channel area ratio and effects from geometrical flow convergence in the radial direction. At early times a "tulip" flame is formed in the circular channel, but not in the Cartesian channel, for the same reasons as the higher rate of acceleration.

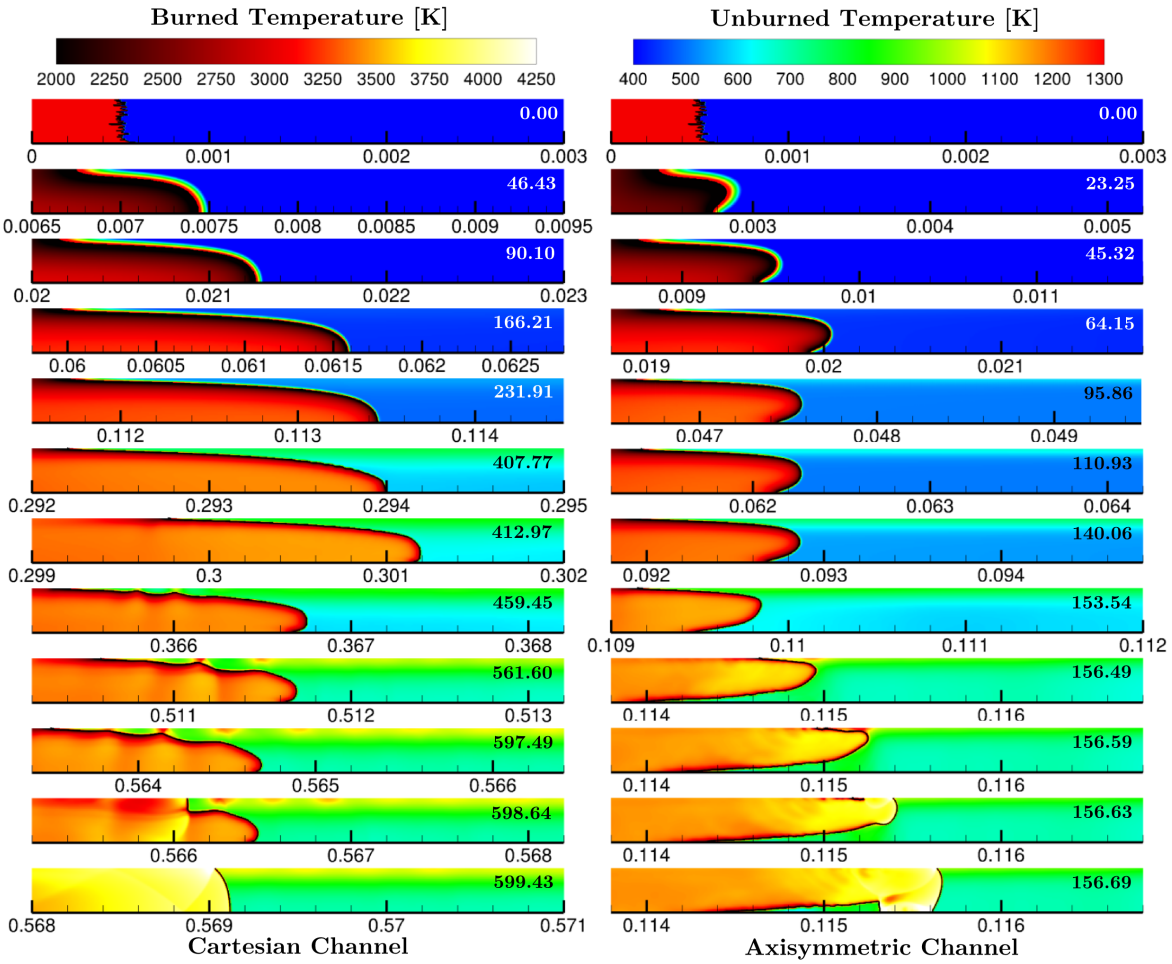

Figure 2: Time-sequence of the flame as it accelerates and transitions to detonation for (left) Cartesian channel and (right) circular channel. Time, in μs, is reported in the upper right of each panel. Distances on the x-axis are reported in meters. The two color scales at the top correspond to the temperature of the burned and unburned material in each panel.

As the flame accelerates, it generates acoustic waves that coalesce into a precursor shock (which is shown in Fig. 3, but does not fit into the frames in Fig. 2). Acoustic waves combine with the axial pressure drop produced from the boundary layer to create a large axial pressure gradient in the reactants. The peak pressure is located immediately in front of the flame tip as a result of the axial pressure gradient in the reactants and acceleration of products through the flame as shown in the pressure profiles in Fig. 3. Viscous dissipation and conversion of kinetic to sensible energy in the boundary layer lead to higher temperatures at the wall than in the core of the channel. For example, in the Cartesian channel at a time of the 407 μs the temperatures just ahead of the flame tip are 583 and 790 K at the centerline and near the wall, respectively.

The flame acceleration ratio of the circular tube to the planar channel, σ_{rat}, is around 3.17, which is higher than the value of 2.1 predicted by theory [20]. The precursor shock, not accounted for in the analysis [20], forms sooner and is stronger in the circular channel (see Fig. 3 at times of 111 and 166 μs for the axisymmetric and Cartesian channels, respectively). The effects of which produce a higher value of σ_{rat} than predicted.

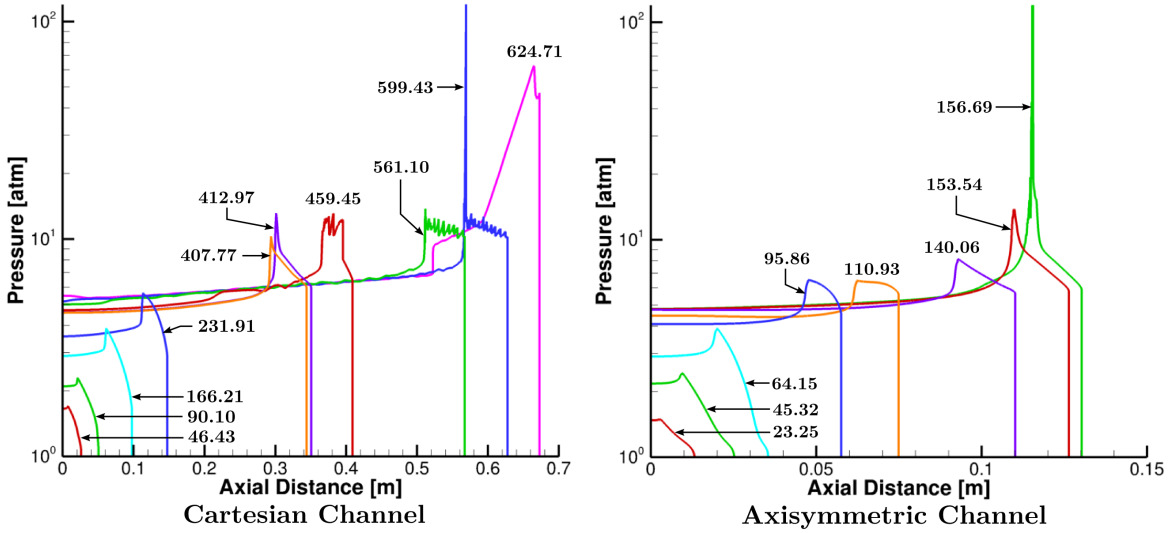

Figure 3: Computed pressure profiles along the centerline of the channel for (left) the Cartesian and (right) the circular cases. The time for each pressure trace is displayed in units of μs.

Our simulations show that the flame speed approaches the Chapman-Jouget deflagration condition and the products become choked with respect to the flame. At a time of 156.35 μs the absolute velocity of the flame tip is approximately 2130 m/s in the circular channel. The flame speed relative to the flow, depending on how the fluid velocity is selected, is 200 ± 15 m/s and the product velocity relative to the flame is $\sim$1500 m/s, which is close to the sound speed. At this time the flame is either choked or nearly choked in the circular channel.

As discussed earlier, pressure rapidly builds at the tip of the flame when it becomes choked. This pressure buildup is strong enough in the circular channel to cause a transition to detonation in a manner similar to what was observed by Ivanov *et al.* [10]. At around a time of 407 μs a similar pressure rise occurs in the Cartesian channel, but a detonation is not formed and an inert shock propagates away from the flame (see Fig. 3 at times of 413 and 459 μs). Shocks travel at a faster speed in burned material than in the unburned reactants. Thus, oblique shocks are formed when pressure waves propagating through the burned material interact with the unburned material near the wall (see Fig. 2 at a time of 562 μs). Reflections of these oblique shocks generate hot-spots in the high-temperature boundary layer. The reactivity gradients inside most of these hot spots are not sufficient to generate a detonation, but produce decoupled shocks and flames (as shown by the bumps on flame surface after 450 μs). Each of these subsequent shocks compresses the reactants little-by-little and also reflect off walls, generating more hot spots in the boundary layer. Near a time of 598 μs the reactivity gradient near a hot spot is sufficient to produce a detonation. The detonation mechanism involving hot spots for the rectangular channel is substantially different than the DDT mechanism observed in the circular channel.

4 Conclusions

We have simulated flame acceleration and deflagration-to-detonation transition of a stoichiometric H_2/O_2 mixture in a thin, 0.5 mm channel using the detailed chemical reaction mechanism of Burke *et al.* [13]. The computed results show that detonation in Cartesian geometry can be initiated in a manner similar to classical hot spot-based mechanisms; however, detonation in circular channels was initiated by pressure build up at the tip of the flame similar to runaway mechanisms proposed for fast flames [6, 7]. A similar

pressure buildup leading to DDT in thin Cartesian channels using a different chemical reaction mechanism was reported by Ivanov *et al.* [10]. The results of these simulations show that the exact mechanism of DDT is heavily dependent on the geometrical setup and the specific chemical reaction mechanism.

References

[1] G. Ciccarelli, S. Dorofeev, Prog. Energy Combust. Sci. 34:499–550 (2008).

[2] A.M. Khokhlov, E.S. Oran, Combust. Flame 119:400–416 (1999).

[3] E.S. Oran, A.M. Khokhlov, Philosophical Transactions of the Royal Society of London A, 357:3539–3551 (1999).

[4] V.N. Gamezo, A.M. Khokhlov, E.S. Oran, Combust. Flame 126:1810–1826 (2001)

[5] Ya.B. Zeldovich, V.B. Librovich, G.M. Makhviladze, G.I. Sivashinsky, Acta Astronaut. 15:313–321 (1970)

[6] A.Y. Poludnenko, T.A. Gardiner, E.S. Oran, Phys. Rev. Lett. 107:054501 (2011)

[7] V.N Gamezo, A.Y. Poludnenko, E.S. Oran, Proc. of 23rd ICDERS (2011)

[8] V.N. Gamezo, E.S. Oran, AIAA Journal, 44:329–336 (2006)

[9] E.S. Oran, V.N. Gamezo, Proc. of 20th ICDERS (2005)

[10] M.F. Ivanov, A.D. Kiverin, M.A. Liberman, Phys. Rev. E 83:056313 (2011)

[11] M.-H. Wu, W.-C. Kuo, Combust. Flame 159:1366–1368 (2012).

[12] R.W. Houim, K.K. Kuo, J. Comput. Phys. 230:8527–8553 (2011).

[13] M.P. Burke, M. Chaos, Y. Ju, F.L. Dryer, S.J. Klippenstein, Int. J. Chem. Kinetics 44:444-474 (2012).

[14] B.D. Taylor, D.A. Kessler, V.N. Gamezo, E.S. Oran, Proc. Combust. Inst. 34:2009–2016 (2012).

[15] P. MacNeice, K. Olson, C. Mobarry, R. de Fainchtein, C. Packer, Computer Phys. Comm. 126:330–354 (2000).

[16] R. J. Spiteri, S. J. Ruuth, SIAM J. on Numer. Anal. 40:469–491 (2003).

[17] J. G. Verwer, B. P. Sommeijer, W. Hundsdorfer, J. Comput. Phys. 201:61–79 (2004).

[18] D.R. Mott, E.S. Oran, B. van Leer, J. Comput. Phys. 164:407–428 (2000) .

[19] G. Bryne, S. Thompson, Vode_f90 support page, http://www.radford.edu/ thompson/vodef90web/ (December 2010).

[20] D.M. Valiev, V. Akkerman, M. Kuznetsov, L.-E. Eriksson, C.K. Law Combust. Flame 160:97–111 (2013).